Micromagnetics of thin film cobalt-based media for magnetic recording

R. Giles, P. S. Alexopoulos, and M. Mansuripur

Citation: Computers in Physics **6**, 53 (1992); doi: 10.1063/1.168445
View online: https://doi.org/10.1063/1.168445
View Table of Contents: https://aip.scitation.org/toc/cip/6/1
Published by the American Institute of Physics

Micromagnetics of thin film cobalt-based media for magnetic recording

R. Giles
College of Engineering, Boston University, Boston, Massachusetts 02215

P. S. Alexopoulos
IBM Almaden Research Center, 650 Harry Road, San Jose, California 95120

M. Mansuripur
Optical Sciences Center, University of Arizona, Tucson, Arizona 85721

(Received 13 December 1990; accepted 23 September 1991)

Methods of fabrication and characterization for thin films of CoCr, CoPt, CoPtCr, and similar alloys of interest in longitudinal magnetic recording are reviewed and certain interesting features of their magnetic behavior, revealed recently with modern high-resolution observation techniques, are described. The micromagnetics of these polycrystalline thin film media has been studied by large-scale simulations on the massively parallel Connection Machine. Methods and results of these simulations are presented.

INTRODUCTION

High-density magnetic recording is currently an active area of research and development around the world. Recent advances in thin-film disk fabrication have brought the achievable densities of longitudinal recording within the range of 10^8 bits/cm^2 (Ref. 1). These densities have been made possible in part by a better understanding of the micromagnetics of thin films. Polycrystalline films of CoX (i.e., CoCr, CoPt, CoPtCr, CoNiCr, etc.) are sputter deposited on chromium-coated substrates, and control of microstructure is achieved through the control of the sputtering process as well as substrate treatment. In the meantime, characterization tools and techniques have steadily improved so that, in addition to high-accuracy bulk measurement techniques (such as vibrating sample and torque magnetometry, ferromagnetic resonance, x-ray diffractometry, etc.), there is now a variety of tools available for micromagnetic characterization of thin film materials. Lorentz electron microscopy can yield high-resolution photographs of the magnetic ripple structure.[2,3] Electron diffraction patterns shed light on the distribution of the magnetization vector with the resolution of electron microscopy. Magnetic force microscopy[4] and Hall microprobe analysis allow measurement of stray fields with a few hundred angstroms of resolution. These developments in turn have made it possible to make informed speculations about the role of various micromagnetic interactions within individual grains and/or among them. In time we shall have the experimental evidence to accept or reject some of the hypotheses and theories that are now being put forward. In this undertaking computer simulations promise to be extremely valuable tools. It is now possible to simulate a reasonably large lattice of crystallites by first computing their interaction fields and then allowing their individual magnetic dipoles to arrive at a local minimum of energy by either following the dynamic laws of magnetization or else through some sort of energy minimization scheme.[5-8] In both cases, micromagnetic features of the lattice (such as ripple structure, nucleation site density, stray field pattern, etc.) as well as macromagnetic characteristics (such as hysteresis loops and torque curves) can be computed and compared with experimental observations. In this way the investigator can test the validity of his hypotheses such as those involving the distribution of anisotropy axes among the grains, the strength of exchange interaction between neighboring crystallite pairs, and the effect of magnetic or structural defects on observable properties of the films.

Large-scale computer simulations that faithfully represent the physics of magnetic interactions without unjustifiable assumptions and approximations have only recently appeared on the scene.[7,8] The reason for this late arrival is that the required computing power has not been available in the past. The Connection Machine, in particular, is perhaps the single most important device for this type of simulation.[9,10] The fact that a 256×256 lattice of dipoles can be directly represented by the 65536 processors of the Connection Machine, and that these processors can inquire about the state of their neighbors in parallel and in minimum communication time, makes the machine uniquely suitable for micromagnetic simulations. Also important in this respect is the fact that fast Fourier transforms, needed for demagnetizing field calculations, can be computed on the Connection Machine much more rapidly than on any available sequential machine.

In this paper we present results of simulations performed on the Connection Machine for thin films of CoX magnetic materials, and compare some of these results with the available experimental data. Microstructural and micromagnetic characteristics of the media of interest are discussed in Sec. I. The micromagnetic theory employed in this work is briefly reviewed in Sec. II, and certain features

of the implementation algorithm are described in Sec. III. Finally, results of computer simulations are presented in Sec. IV.

I. STRUCTURAL AND MAGNETIC CHARACTERISTICS OF THE MEDIA

High-performance magnetic recording media have traditionally been designed using a criterion based on the transition width parameter α, where

$$\alpha \simeq M_r h / H_c. \tag{1}$$

In the above expression h is the film thickness, while M_r and H_c are the remanent magnetization and the coercivity of the medium, respectively.[11] As a general rule, higher linear densities are achieved when the transition width is made smaller. On the other hand, the read signal is proportional to the medium's magnetization, and the required recording field must increase if the coercivity of the medium is raised. These requirements impose conflicting constraints on the media characteristics and call for many compromises in the design of the magnetic recording media.

As far as thin film media are concerned, cobalt is the material of choice because of its high saturation magnetization, mechanical properties, and ease of fabrication. Unfortunately, cobalt in pure form has very low coercivity and relatively poor corrosion resistance. In order to provide the desired range of coercivities and enhanced corrosion resistance, cobalt has been alloyed with other elements. The most commonly used elements in binary and ternary alloys of cobalt for magnetic recording applications are Cr, Ta, Ni, Pt, Pd, and W.

The saturation magnetization M_s and the coercivity H_c of CoX alloys can be tailored to specific needs through the control of composition, deposition parameters, and substrate material texture.[1,12–15] In CoPt alloys, for instance, coercivity is roughly a linear function of the atomic percentage of platinum, ranging from 200–2000 Oe as the platinum content of the alloy increases from zero to 20%. It should be emphasized, however, that the coercivity of a given alloy is also controlled by its microstructure (including grain size, defect density, nature of grain boundaries, etc.), the strength of its crystalline anisotropy, the distribution of its anisotropy axes among the grains, residual stresses, and so on.[16]

In recent years it has become clear that, while the macroscopic parameters are useful for media development, they are not adequate for predicting the functional performance of the recording media. Thin film disks with similar macromagnetic parameters (such as H_c, M_s, remanent squareness S, and coercivity squareness S^*) can have dramatically different signal to noise ratios, a fact that may be appreciated by considering the data shown in Fig. 1. This figure compares the performance of two thin film media, one based on CoPt and the other on CoPtCr magnetic alloys. These media, while macroscopically similar, are indeed very different in terms of their readout signal and noise characteristics.

Investigation of noise for a number of cobalt alloy films has shown an increase of media noise with the increasing linear bit density. This feature has been associated

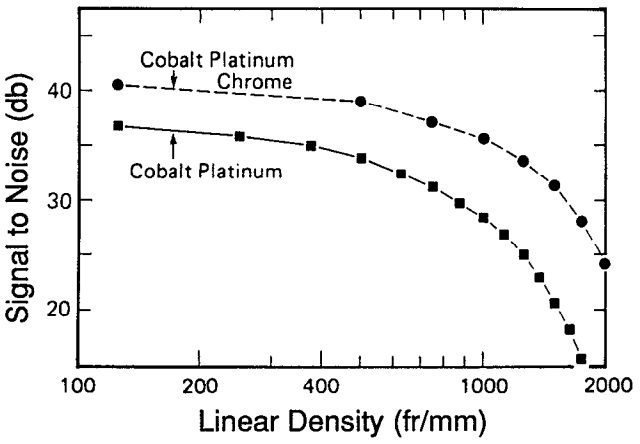

FIG. 1. Signal-to-noise ratio versus linear recording density (in flux reversals per millimeter) for two cobalt-based thin film disks. Although the macromagnetic characteristics of the two media are comparable, differences in micromagnetic behavior cause the transition noise in the CoPtCr alloy to be substantially below that of the CoPt alloy.

with the noise generated at the transition region between adjacent magnetic domains.[17,18] Observation of recorded transitions on a series of CoX alloys by Lorentz electron microscopy has shown complex domain wall structures dominated by ripples, vortices, and featherlike micromagnetic features.[19] A typical example of such structures is shown in Fig. 2. Vortices, ripples, and feathers that have been identified at scales down to a few nanometers are presently believed to arise from local minimization of magnetic energy, which is given by

$$E_{\text{total}} = E_{\text{exchange}} + E_{\text{anisotropy}} + E_{\text{demagnetization}}. \tag{2}$$

The exchange interaction in polycrystalline films has two components. The first component is interatomic and oper-

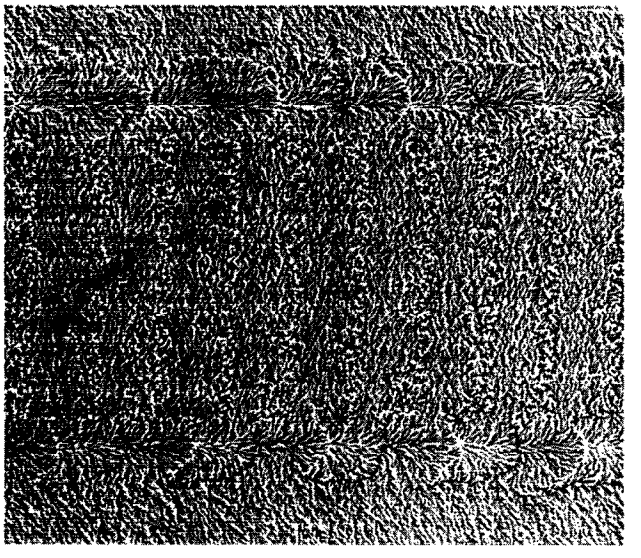

FIG. 2. Lorentz electron micrograph (Fresnel mode) of transition regions in a cobalt-based alloy. The transitions were recorded with an inductive head at approximately 1 μm intervals. Ripples, vortices, and feather like structures are clearly visible in this picture.

ates within individual grains, while the second component is intergranular and resides in the interaction between neighboring crystallites. The main contribution to anisotropy energy comes from crystalline anisotropy which, for cobalt alloys, is strong and uniaxial, with the magnetic easy axis of individual grains coinciding with their crystallographic c axis. (The other component of anisotropy, which is rather small for cobalt alloys of interest, is stress induced and, to a good approximation, may be ignored in micromagnetic analyses.) X-ray diffraction studies of CoX media indicate that the crystallographic c axes of the grains are randomly oriented, with little or no correlation among the neighboring grains. There is, however, a tendency for the c axes to be in the plane of the film rather than perpendicular to it. Figure 3 shows the x-ray diffraction pattern for a 230 Å-thick layer of $Co_{70}Pt_{12}Cr_{18}$ alloy film deposited on a chromium underlayer. Three CoPtCr peaks corresponding to hcp (10.0), (00.2), and (10.1) are identified in the figure after deconvolution. The peaks are broad and low intensity. The (10.0) and (10.1) peaks are dominant with a relatively weak (00.2) peak, indicating a degree of preference for the c axis to lie in or near the plane of the film. The grain size, estimated from the width of the (10.0) peak and verified by TEM is about 180 Å (Ref. 1).

The micromagnetic feature size is determined by the competition between the exchange and magnetostatic forces, on the one hand, and the strength of local anisotropy, on the other. While exchange and classical dipole–dipole interactions prefer the magnetic alignment of grains, local anisotropy favors the random spatial distribution of these dipole moments. Parameters that influence the various energies in Eq. (2) may be controlled through the composition and microstructure of the film in a number of ways including chemical alloying, use of nucleating underlayers, and control of deposition parameters. In the case of dense-continuous films, since exchange and magnetostatic interactions are both proportional to the saturation moment of the material, any reduction of M_s by chemical alloying (with Cr, Pt, Ni, etc.) will likely result in a reduction of magnetic coupling. Alloying may also result in grain boundary segregation that affects the strength of intergranular exchange. At the same time, alloying could increase the strength of local (crystalline) anisotropy, resulting in higher coercivities and finer ripple structures.

Another approach to reducing the intergranular exchange coupling is the physical separation of adjacent grains or clusters of grains. This approach results in small single-domain regions to the extent that, in extreme cases, each grain itself may constitute an individual domain. Physical separation of grains can be achieved through the control of deposition environment, utilization of an underlayer material with appropriate thickness, and/or post-deposition processing. Transmission electron micrographs of samples produced with varying degrees of grain separation are shown in Fig. 4. The Thornton diagram[20,21] for sputtered films shows that, depending on the deposition parameters (e.g., sputtering gas pressure, deposition rate, substrate temperature, film thickness, atomic mass of the sputtering gas), one can obtain either dense-continuous or columnar-porous films. Deposition of the magnetic film on a porous columnar underlayer results in a medium with physical separation of grains. Incorporation of alloying effects and polycrystalline epitaxy on physically separated columns can further enhance the ability to tailor the microstructure of the media.

Figure 5 shows the hysteresis loops, obtained in a vibrating sample magnetometer, for thin CoPtCr alloy films. The two compositions depicted in this figure are

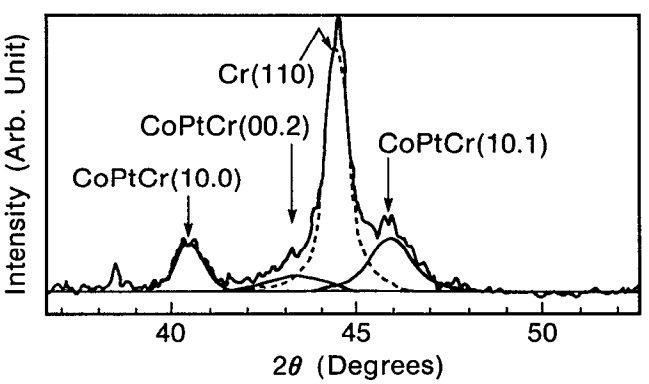

FIG. 3. Shown is the x-ray diffraction pattern for a 230 Å-thick film of CoPtCr alloy on a chromium underlayer. The bcc (110) peak of the Cr underlayer is the strongest, but the hcp (10.0), (10.1), (00.2) peaks of CoPtCr are also clearly present. The (10.0) peak represents grains whose c axes are in the plane of the film, while the (10.1) peak corresponds to those grains with the c axis at an angle from the film plane.

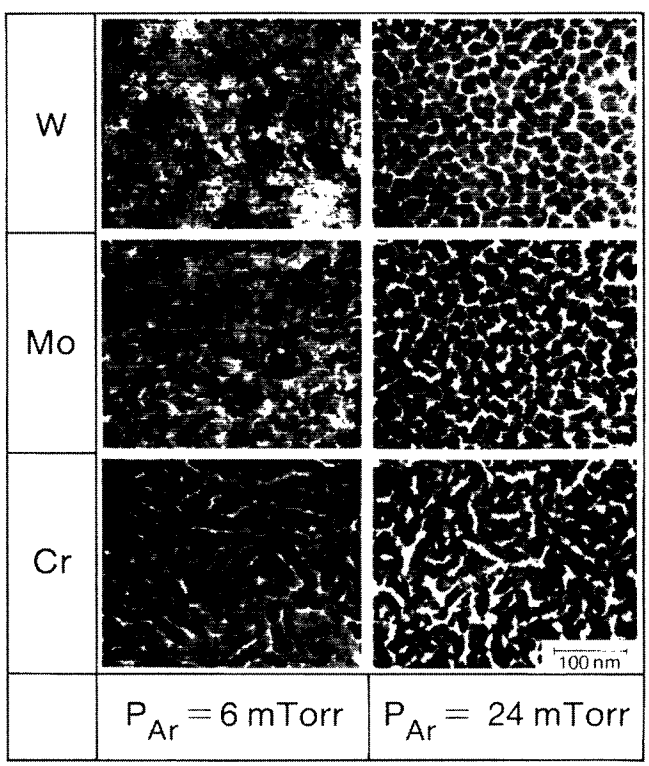

FIG. 4. Plane-view TEM micrographs of CoPtCr grains on Cr, Mo, and W underlayers, deposited at 6 mTorr (left column) and 24 mTorr (right column). Note that the grains tend to be well defined and isolated as the pressure of the sputtering gas increases (courtesy of Dr. Thao Nguyen, IBM Corporation).

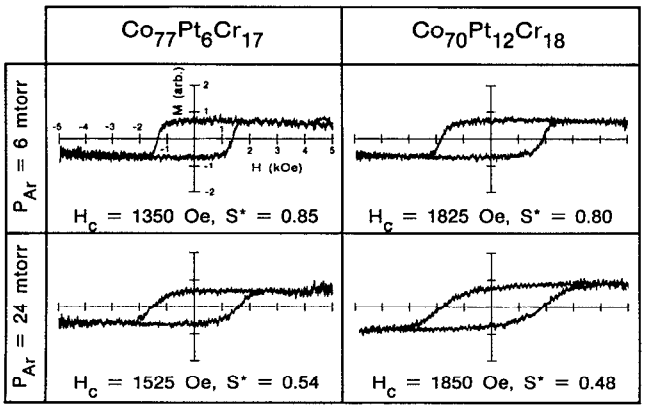

FIG. 5. Hysteresis loops for two compositions of CoPtCr alloy, each deposited at two different sputtering pressures (from Ref. 1).

$Co_{77}Pt_6Cr_{17}$ and $Co_{70}Pt_{12}Cr_{18}$, each prepared at two different sputtering gas pressures.[1] One observes that the composition with higher percentage of platinum has higher coercivity, but perhaps more important is the fact that samples fabricated under high argon pressure have reduced values of coercivity squareness S^*. As observed in Fig. 4, high-pressure sputtering results in columnar growth and decoupled grains, which are in turn responsible for the low values of S^*. This relationship between the strength of intergranular coupling and the shape of the hysteresis loop has been confirmed in the past both by theoretical calculations and by computer simulations,[5,8] and will be further explored in Sec. IV of the present paper.

Lorentz electron micrographs showing the morphology of the magnetic state at various points along the hysteresis loop are shown in Fig. 6.[22] The sample depicted here is a thin film of $Co_{90}Pt_{10}$ alloy. The hysteresis loop for this sample is shown in the upper-left-hand corner of the figure, and the state of remanent magnetization (point *a* on the loop) is revealed by the Fresnel micrograph in frame (a). During the experiment a reverse field was applied and the state of magnetization was brought to point *b*, before the field was returned to zero. The morphology of the magnetization pattern in this new remanent state is shown in frame (b). The remaining micrographs in frames (c), (d), and (e) are obtained in similar fashion and represent the morphology of the state corresponding to points *c*, *d*, and *e* on the hys-

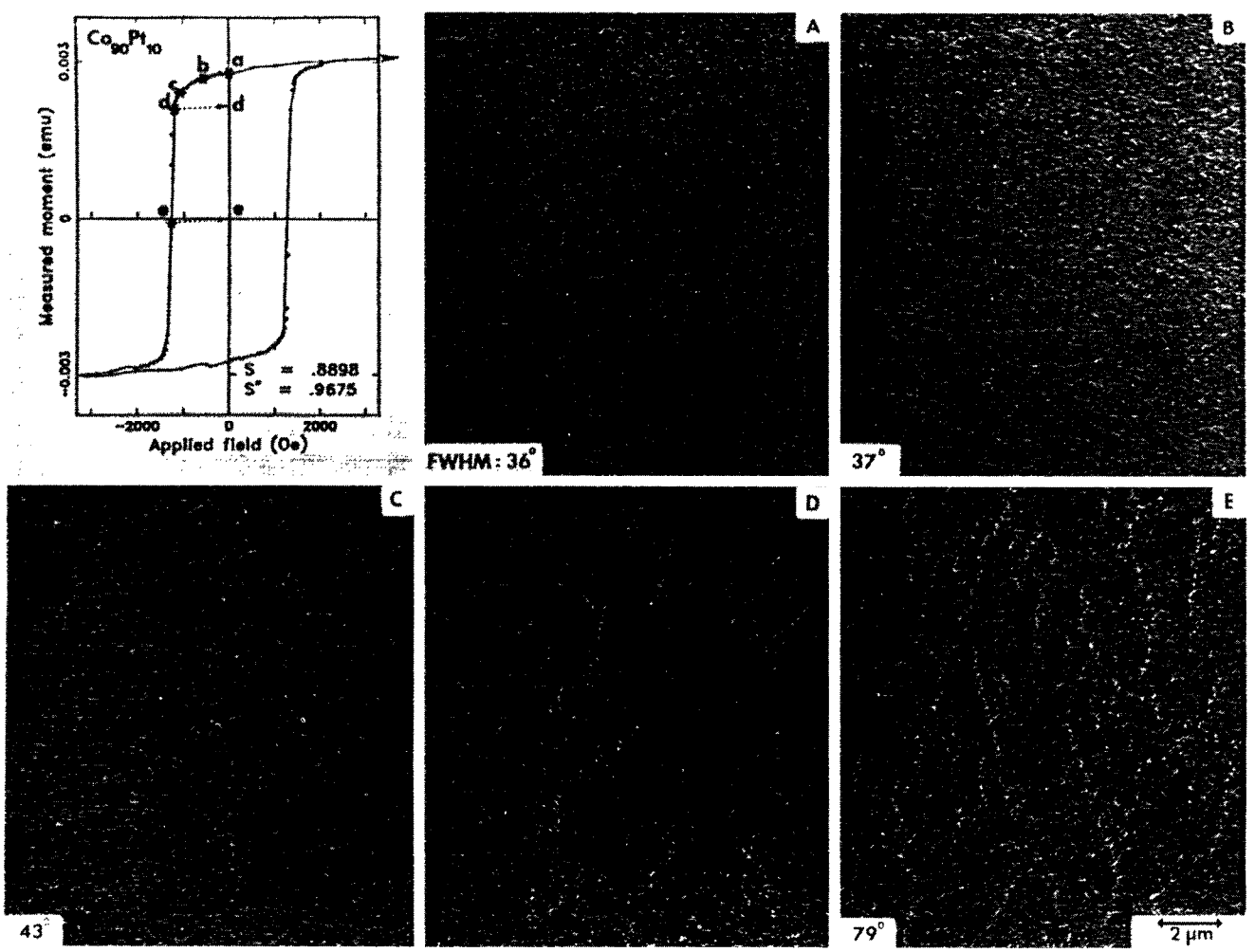

FIG. 6. Lorentz electron micrographs (Fresnel mode) showing the morphology of the magnetic state at various points along the hysteresis loop. Frames (a)–(e) correspond, respectively, to points a–e on the loop (courtesy of Dr. Thao Nguyen, IBM Corporation).

teresis loop. Note that the reversal proceeds by nucleation and growth of reverse-magnetized domains, and that these domains, as shown in frames (d) and (e), are elongated in the direction of the applied field. Similar features are exhibited by our large-scale computer simulations which will be described in Sec. IV.

II. MICROMAGNETIC THEORY

The phenomenological equation of Landau, Lifshitz, and Gilbert (LLG equation) is the basis of our computer simulations.[23-26] According to the LLG equation, a magnetic dipole $\mathbf{m}$ in an effective magnetic field $\mathbf{H}_{\text{eff}}$ follows a damped gyration path to equilibrium. The damping coefficient α is dimensionless and the time rate of change of $\mathbf{m}$ is related to $\mathbf{H}_{\text{eff}}$ and α as follows:

$$\dot{\mathbf{m}} = \gamma \mathbf{m} \times \mathbf{H}_{\text{eff}} + (\alpha/|\mathbf{m}|)\mathbf{m} \times \dot{\mathbf{m}}, \tag{3}$$

where γ is the gyromagnetic ratio and $\dot{\mathbf{m}} = d\mathbf{m}/dt$. Notice that in the absence of damping (i.e., when $\alpha = 0$) the dipole moment $\mathbf{m}$ gyrates around the field vector $\mathbf{H}_{\text{eff}}$, just like any object with angular momentum $\mathbf{m}/\gamma$ would in response to a torque $\mathbf{m} \times \mathbf{H}_{\text{eff}}$. The effect of damping is to continuously reduce the radius of gyration until $\mathbf{m}$ aligns itself with $\mathbf{H}_{\text{eff}}$.

To simulate the magnetization dynamics of thin film CoX alloys, we made several assumptions. First, we assumed that each crystallite or grain of the material acts as a single domain particle; in other words, we assumed that the exchange forces within a grain are far stronger than any other force that might act on the grain's individual atomic dipoles. Given the strong Co–Co exchange interaction, this assumption is reasonable so long as the grains under consideration are fairly small. Second, we assumed that the grains are equal in size and shape, and are regularly distributed on a two-dimensional hexagonal lattice. The film thickness h is constant and the magnetization throughout the thickness was assumed to be uniform. Figure 7(a) shows the postulated geometry of the grains and their placement in the lattice; each grain is a hexagonal-base prism of height h. If the lattice constant in Fig. 7(a) is denoted by d, the grain volume will be given by

$$V = (\sqrt{3}/2)d^2h. \tag{4}$$

The saturation magnetization M_s of the material can be measured in a vibrating sample magnetometer (VSM). If the assumption is made that the grains are densely packed, then the magnitude of the dipole moment assigned to each lattice cell will be

$$|\mathbf{m}| = M_s V. \tag{5}$$

The effective field $\mathbf{H}_{\text{eff}}$ acting on each dipole in the lattice has contributions from at least four different sources. These sources and their corresponding fields are discussed separately in the following paragraphs.

A. Anisotropy

Each grain is assumed to have uniaxial magnetic anisotropy of strength K_u. The anisotropy energy density is given by

$$E_k = -K_u[\mathbf{u} \cdot (\mathbf{m}/|\mathbf{m}|)]^2, \tag{6a}$$

where $\mathbf{u}$ is a unit vector representing the local axis of anisotropy. The effective field corresponding to anisotropy is derived from Eq. (6a) and is given by[26]

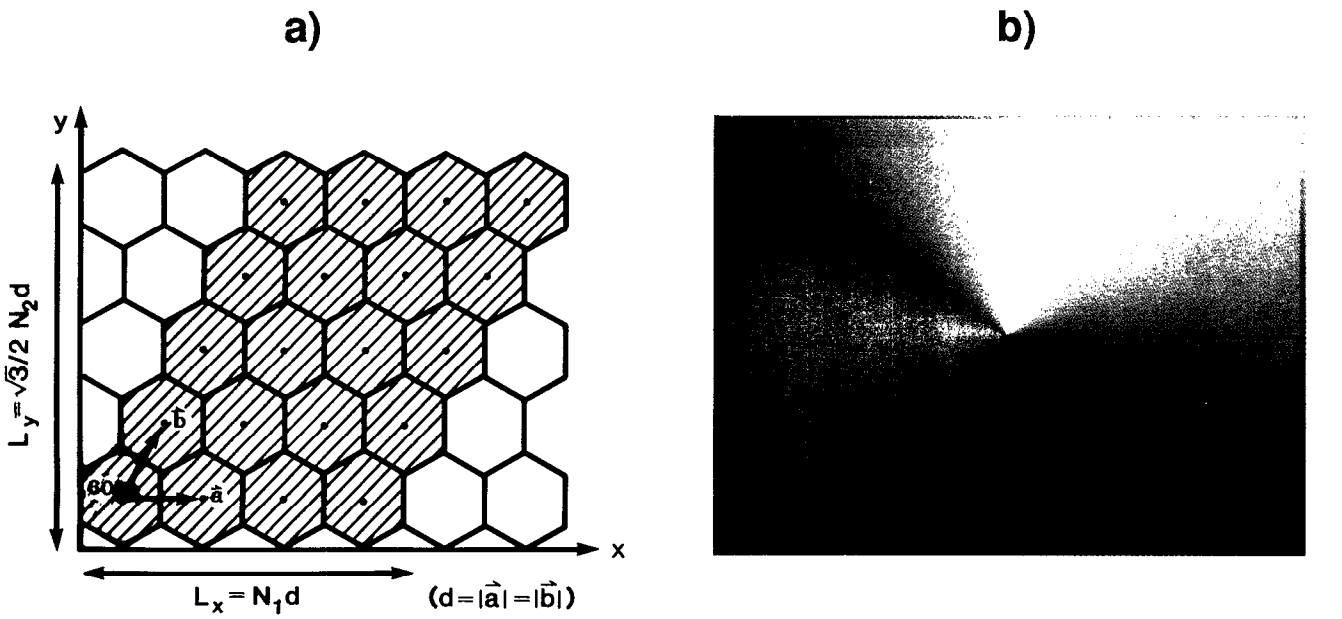

FIG. 7. (a) Geometry of the lattice. Each hexagonal cell represents a crystallite or grain of the actual film. The basis vectors **a** and **b** have equal lengths d, which is referred to as the lattice constant. (b) The color wheel. A two-dimensional vector field in a plane (such as the distribution of magnetization directions in the XY plane of the lattice) is color coded by assigning each pixel the color corresponding to the direction of the local field. In this coloring scheme, red corresponds to the $+X$ direction, green to $+Y$, blue to $-X$, and purple to $-Y$. Alternatively, the color wheel may be used to represent a scalar field in the XY plane. For example, if the field assumes values in the range $[-1, +1]$, then red is assigned to -1 and purple to $+1$, with the intermediate colors (yellow, green, blue,...) assigned sequentially to the values between -1 and $+1$.

$$\mathbf{H}_k = (2K_u/M_s)[\mathbf{u}\cdot(\mathbf{m}/|\mathbf{m}|)]\mathbf{u}. \quad (6b)$$

Each grain is allowed to have its own axis of anisotropy and, for all the results reported here, the axes were assigned randomly either in the plane of the lattice (2 D) or on the unit sphere (3 D).

B. Exchange

Neighboring grains interact at their common boundary by means of exchange forces. The strength of this interaction depends on the grain material, separation between the grains, and the composition and structure of the material in the boundary region. Since little quantitative information regarding the strength of exchange is available from the experimental measurements, we have chosen to treat it as an adjustable factor. The effective exchange field on a given dipole $\mathbf{m}$ due to a neighboring dipole $\mathbf{m}'$ will be denoted by $\mathbf{H}_{xhg}$ whose magnitude is an adjustable constant and whose direction is that of $\mathbf{m}'$. The magnitude of $\mathbf{H}_{xhg}$ is related to the exchange stiffness constant A_x through the relation[27]

$$|\mathbf{H}_{xhg}| = 8A_x/ZM_s d^2, \quad (7)$$

where Z is the coordination number of a site in the lattice. ($Z = 6$ for the hexagonal lattice used in our simulations.)

C. Demagnetization

Classical dipole–dipole interactions give rise to demagnetizing fields. These fields which significantly influence the magnetic processes of thin film CoX alloys are also the hardest to compute. The difficulty of computation is rooted in the long-range nature of the interaction and the fact that every dipole in the system contributes to the field on all other dipoles. Fortunately, however, there is an elegant solution to the problem of demagnetizing field computation based on fast Fourier transforms.[28,29] FFT computations are particularly suited to the Connection Machine environment where a one-dimensional array of length N can be transformed in a time proportional to $\log N$, as opposed to $N \log N$ which is the corresponding time for conventional sequential machines. The FFT-based algorithm is accurate and, unlike direct dipole–dipole calculations, does not require that film thickness h and lattice constant d be roughly equal.[6] It also avoids the cumbersome integrations that must be carried out in order to go beyond the single dipole approximation of a lattice cell and to compute the average interaction over the volumes of magnetic material within the cells.[30]

The approximations involved in the Fourier technique are those due to discretization and those arising from the imposition of periodic boundary conditions. The first approximation will have a negligible effect if the spatial variations of magnetization over a lattice constant d are kept small. As for the second approximation, in a two-dimensional system the effective range of demagnetizing field is comparable to the film thickness; thus periodicity only affects a narrow region near the boundary of the lattice.

D. External field

The external field $\mathbf{H}_{ext}$ is the fourth contribution to the effective field $\mathbf{H}_{eff}$. This field is simply added to the sum of anisotropy, exchange, and demagnetizing fields in order to yield the total effective field at a given lattice site. Although any spatial distribution of $\mathbf{H}_{ext}$ could be considered in these simulations, we studied only the effect of uniform magnetic fields; thus the hysteresis loops and torque curves described in Sec. IV were obtained by relaxing the system of dipoles in the presence of an external field which was uniform over the entire lattice. As for the time dependence of $\mathbf{H}_{ext}$, two strategies were devised. In one strategy the field was kept constant until the lattice reached equilibrium. The field was then incremented by a finite amount, and the lattice was relaxed again. The process continued until a sufficient number of points for either the hysteresis loop or the torque curve was obtained. The second strategy consisted of changing $\mathbf{H}_{ext}$ continuously at a fixed rate. This would have been realistic if we had used physically realizable rates, say 1 Oe/ms. Because of the scale of the computations, however, such slow rates were not practical, and we had to use values as large as 1 Oe/ns instead. Nevertheless, as long as the dynamics of the lattice is fast enough (compared with the rate of change of $\mathbf{H}_{ext}$), such artificially high rates could still produce reasonably accurate and meaningful results.

For the remaining parameters of the LLG equation, we chose a gyromagnetic ratio γ equal to -10^7 Hz/Oe, and a damping coefficient α in the range of 0.2–0.5. Here, α was chosen arbitrarily for the lack of reliable experimental data in this area; although the specific value of α used in the simulations does not seem to influence the macroscopic behavior of the lattice in any significant way, it does affect the microstructure of the equilibrium state. This might be understood in light of the fact that the system of dipoles as a whole has many states of local minimum energy, and the particular state in which the system comes to rest depends on the exact path it takes upon departing from the previous state. Larger values of α result in rapid approach to equilibrium, while small values prolong the computer simulations.

III. THE ALGORITHM

Hysteresis loops and torque curves were traced out by relaxing the system of dipoles in a sequence of external fields. In the case of the hysteresis loops, initially a large in-plane field H_x was applied in the negative X direction. The system was started with uniform magnetization along $-\hat{x}$ and allowed to relax. Then the field H_x was increased and the system relaxed again. In the case of the torque curves, the procedure was similar, but the field $\mathbf{H}_{ext}$ (with fixed magnitude) rotated either in the plane of the lattice or within a perpendicular plane.

In those simulations where the strategy was to change $\mathbf{H}_{ext}$ in discrete steps, relaxation of the lattice for a given value of the field was accomplished by evolving the LLG equation through 500–1000 integration steps, corresponding roughly to a total elapsed time of 0.5 to 1.0 ns. The time interval Δt per integration step was chosen such that no magnetization vector rotated more than 1° per integration step. After this first phase of relaxation, a conjugate-gradient energy minimizer was used to find a nearby, locally minimum state of energy. This second phase of energy minimization substantially accelerated the convergence to

an equilibrium state. Figure 8 shows the effect of the conjugate-gradient minimizer relative to LLG dynamics. This particular run corresponds to a system with $M_s = 900$ emu/cm^3, $H_k = 4000$ Oe, $H_{xhg} = 100$ Oe, 2-D random distribution of the anisotropy axes, and $\alpha = 0.2$. The applied field H_{ext} was 1500 Oe along the positive X axis. Initially, the sample was demagnetized and its average magnetization along X was $\langle M_x \rangle \simeq 0$. With an increasing number of iterations, $\langle M_x \rangle$ approached a final value around 0.77 M_s. The various curves in Fig. 8 correspond to different runs with the same initial state and external field, but with switchover to the conjugate-gradient minimizer after different numbers of steps, ranging from 0–1500. We see that the final magnetization is approximately the same in all cases, and that the final state is achieved after a few tens of conjugate gradient steps as compared with hundreds of additional LLG steps. Note, however, that the states reached are not exactly the same.

When the strategy was to use a continuously varying field, the results depended on the time rate of change of $\mathbf{H}_{ext}$. Here, the LLG dynamics were used throughout, and no attempt was made to reduce the computation time by resorting to the conjugate-gradient technique. Figure 9 shows sections of three hysteresis loops, computed with three different rates, for a lattice with $M_s = 900$ emu/cm^3, $H_k = 4000$ Oe, $H_{xhg} = 300$ Oe, 3-D random anisotropy, and $\alpha = 0.5$. (Only a section of each loop near the coercive field H_c is shown.) Clearly, the coercivity is lower for slower rates of change of $\mathbf{H}_{ext}$; within the range studied, H_c dropped from 937 to 906 Oe. With a continuously varying field, therefore, the calculated H_c may be somewhat of an overestimate.

Because of the frustrations caused by the random axes of anisotropy, the energy surface is expected to have many local minima. Dynamics starting from a particular initial state will pick out a unique minimum, but a slightly different starting point will lead to a different final state. By the same token, switching over to the conjugate-gradient minimizer (or changing the rate of increase or decrease of the applied field) affects the path and, inevitably, the final state of the system. We have found, however, that the bulk properties of all these states are similar, and expect that real materials will be accurately modeled by these simulations. The use of conjugate-gradient minimizer to accelerate convergence is, therefore, acceptable, and, in fact, recommended, in most situations. Also, we found little difference between the results obtained by scanning the field in discrete steps, and those found by varying the field at a fixed rate. The method of scanning the field was therefore selected arbitrarily for each problem, and the results presented in the next section contain examples of both methods.

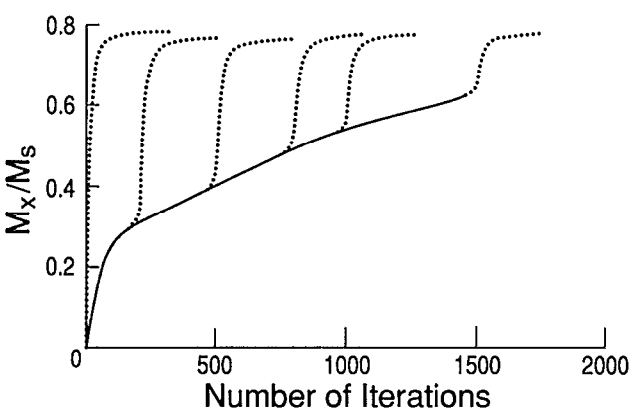

FIG. 8. Magnetization component M_x along the externally applied field H_x for a variety of crossovers from LLG dynamics to the conjugate-gradient energy minimizer.

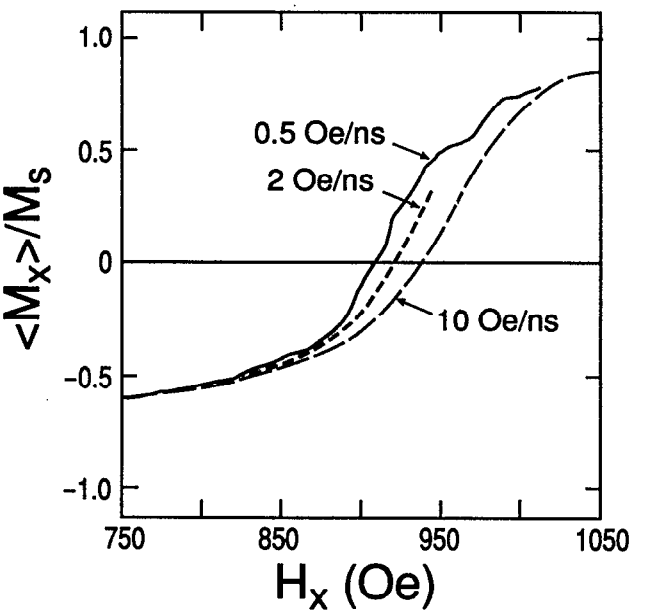

FIG. 9. Sections of the hysteresis loop near the coercive field, obtained using three different rates for scanning the applied field. The solid curve corresponds to a rate of 0.5 Oe/ns, and shows a coercivity of $H_c = 906$ Oe. The other two curves were obtained when H_x was scanned at 2 Oe/ns and 10 Oe/ns, yielding coercivities of 920 and 937 Oe, respectively. Note that the differences among the curves are mainly in the neighborhood of the coercive field; far away from this region, the curves are nearly identical.

The computations were performed on the 16384-processor Connection Machine at Boston University. A 128×128 lattice of dipoles is readily mapped onto the processors in a one-to-one manner. The machine, however, has virtual processing capability that allows the simulation of larger lattices. Our 256×256 lattice, for instance, was mapped by assigning four lattice cells to each processor.

IV. RESULTS AND DISCUSSION

Table I lists the parameter values used in the simulations reported in this section. Detailed descriptions of the various simulations and the corresponding results are presented in the following Examples.

A. Example 1

In the first series of calculations, we traced the hysteresis loops for a fixed anisotropy field of $H_k = 4000$ Oe and various strengths of the exchange interaction. The systems under consideration had 2-D random distributions of anisotropy axes; that is, the axes were random in the plane of the

TABLE I. Simulation parameters.

Parameter	Symbol	Value
Lattice spacing	d	50 nm
Film thickness	h	50 nm
Lattice dimensions	···	256×256
Saturation magnetization	M_s	900 emu/cm^3
Anisotropy field strength	H_k	3000–5000 Oe
Anisotropy axes	···	random in XY or XYZ
Exchange field	H_{xhg}	0–500 Oe
Gilbert damping coefficient	α	0.2–0.5
Gyromagnetic ratio	γ	-10^7 Hz/Oe

film. Figure 10(a)–(f) shows loops for samples with $H_{xhg} = 0, 100, 200, 300, 400$, and 500 Oe, respectively. Here, the applied field was scanned continuously at the rate of 20 Oe/ns for each loop. The first four loops have coercivities in the neighborhood of 1300 Oe, but differ primarily in their remanent squareness S, and the sharpness S^* of the transition region; increasing H_{xhg} sharpens the transition considerably. The last two loops have somewhat lower coercivities, but they have very steep transitions. The values of remanent squareness S for these loops are 0.70, 0.77, 0.81, 0.85, 0.86, and 0.87, respectively. Note that the exchange fields used here are relatively weak (a few hundred Oersteds), as compared with the anisotropy field (4 kOe) and the scale of magnetostatic fields ($4\pi M_s \simeq 11$ kOe).

In general, the basic features of the loops remained unchanged when we increased the size of the lattice, changed the random number seed for generating the axes of anisotropy, or modified the rate of scan of H_x. Also, by applying the external field along several (arbitrarily selected) directions in the XY plane, we confirmed the overall macroscopic isotropy of the lattice.

Figure 11 is similar to Fig. 10 except that the samples studied here had their axes of anisotropy distributed randomly in three-dimensional space. The loops in this figure belong to samples with $H_k = 4000$ Oe, but with different values of H_{xhg}. Comparing the results in Fig. 11 with those in Fig. 10, one notes that the remanent values have remained more or less unchanged, while the coercivities have dropped significantly. Apparently, the reversal process is made easier when the moments are allowed to reverse their direction by rotating out of the plane of the sample. Similar observations can be made for the two loops in Fig. 12 which represent samples with $H_k = 3000$ Oe and $H_{xhg} = 100$ Oe, but have their axes of anisotropy distributed randomly in 2 D and 3 D, respectively. The coercivity drops from 850 to 640 Oe but the remanence remains at about 0.76. Finally, Fig. 13 shows loops for samples with $H_k = 5000$ Oe and $H_{xhg} = 100$ Oe. The sample with 2-D random anisotropy has $H_c = 1670$ Oe and $M_r = 0.75\ M_s$, while the sample whose axes are random in 3 D has $H_c = 1440$ Oe and $M_r = 0.7\ M_s$.

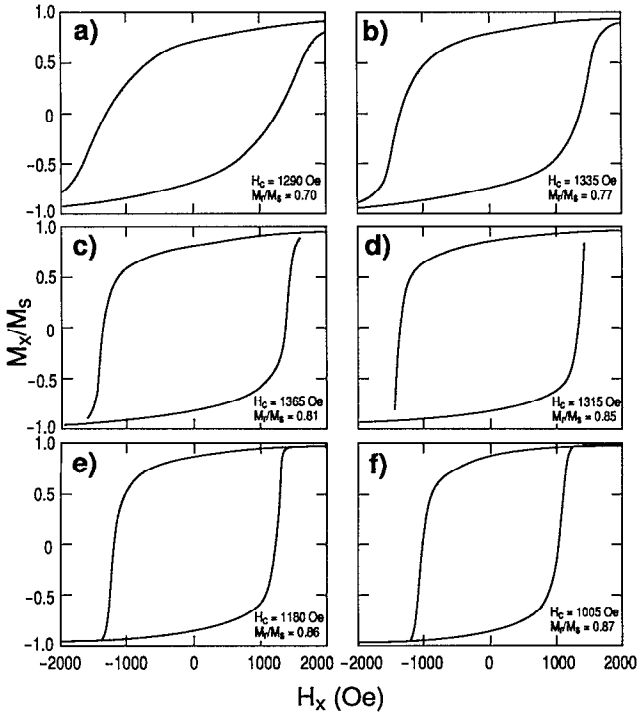

FIG. 10. Hysteresis loops showing M_x versus the applied field H_x for a sample with 2-D random anisotropy, $H_k = 4000$ Oe, and different values of the exchange field H_{xhg}. These loops were obtained by scanning the applied field H_x at the fixed rate of 20 Oe/ns. (a) $H_{xhg} = 0$, (b) $H_{xhg} = 100$ Oe, (c) $H_{xhg} = 200$ Oe, (d) $H_{xhg} = 300$ Oe, (e) $H_{xhg} = 400$ Oe, (f) $H_{xhg} = 500$ Oe.

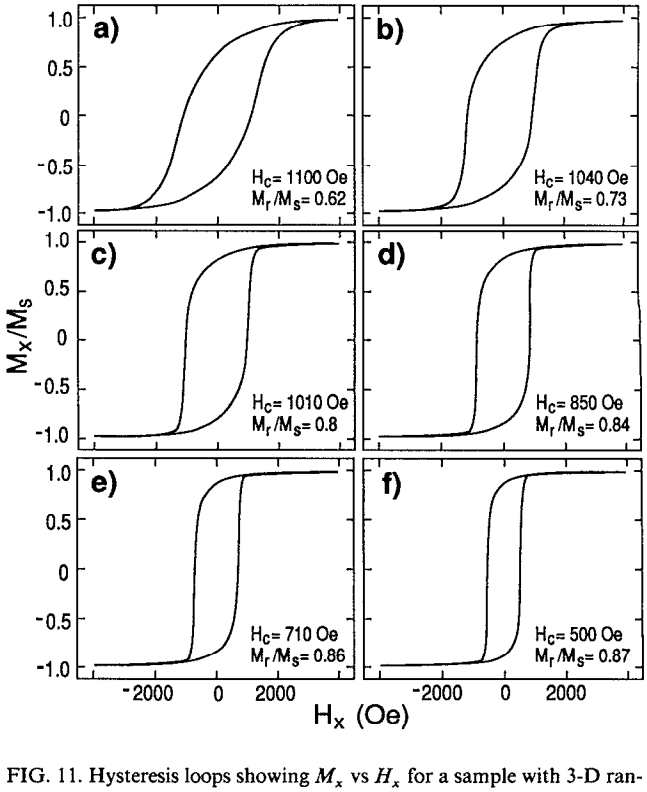

FIG. 11. Hysteresis loops showing M_x vs H_x for a sample with 3-D random anisotropy, $H_k = 4000$ Oe, and different values of the exchange field H_{xhg}. The field scans were done by incrementing H_x in discrete steps, and accelerating the dynamics by using the conjugate-gradient energy minimizer after several hundred LLG steps. (a) $H_{xhg} = 0$, (b) $H_{xhg} = 100$ Oe, (c) $H_{xhg} = 200$ Oe, (d) $H_{xhg} = 300$ Oe, (e) $H_{xhg} = 400$ Oe, (f) $H_{xhg} = 500$ Oe.

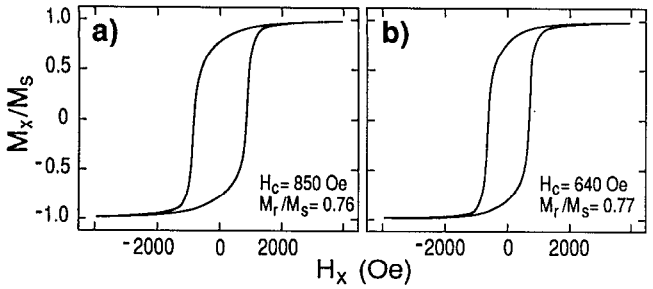

FIG. 12. Hysteresis loops for a sample with $H_k = 3000$ Oe and $H_{xhg} = 100$ Oe. (a) 2-D random anisotropy, (b) 3-D random anisotropy.

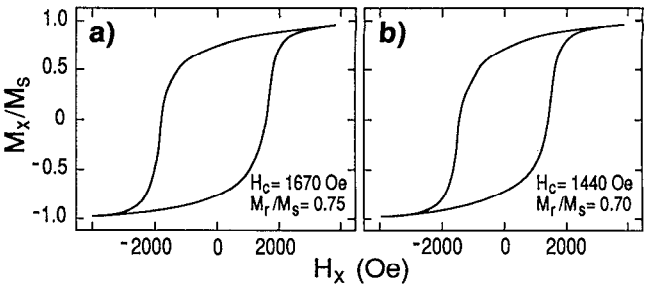

FIG. 13. Hysteresis loops for a sample with $H_k = 5000$ Oe and $H_{xhg} = 100$ Oe. (a) 2-D random anisotropy, (b) 3-D random anisotropy.

The field scan for Figs. 11–13 was done in discrete steps, and the conjugate-gradient energy minimizer followed the LLG dynamics (as described in Sec. IV) to assure that the system reaches steady state before the field is incremented. The curves traced out numerically are quite smooth. This indicates that the step size chosen for H_{ext} is small enough to allow near-continuous behavior, and that the lattice is sufficiently large to effectively average out the fluctuations caused by the random assignment of local anisotropy axes.

B. Example 2

The state of magnetization of the lattice was monitored during the loop tracings, and displayed in color graphics. A vector field in two-dimensional space can be displayed with the aid of the color wheel [see Fig. 7(b)]. A blue pixel indicates that the corresponding magnetization vector is in the $-X$ direction, while a red pixel is along $+X$. Similarly, the magnetization of green and purple pixels is in the $+Y$ and $-Y$ directions, respectively. Figure 14 shows the patterns of magnetization during the reversal of a sample with 2-D random anisotropy, $H_k = 4000$ Oe and $H_{xhg} = 300$ Oe. The hysteresis loop for this sample is shown in Fig. 10(d). Each frame in Fig. 14 is obtained at a different value of the applied field, starting with $H_{ext} = -600$ Oe in (a), and increasing to 800 Oe at (b), to 1155 Oe at (c), to 1310 Oe at (d), to 1375 Oe at (e), and to 1465 Oe at (f). For clarity, the magnified view of a small region in each frame is also displayed in the figure. We observe that regions of reversal form long "fingers" at more or less regular intervals, which eventually expand to fill the entire plane of the sample. There are clearly regions that are weakly bound and reverse rapidly, and other regions that may be identified as stiff, since they resist reversal until the applied field has reached large values.

Figure 15 shows the angular distribution of the mag-

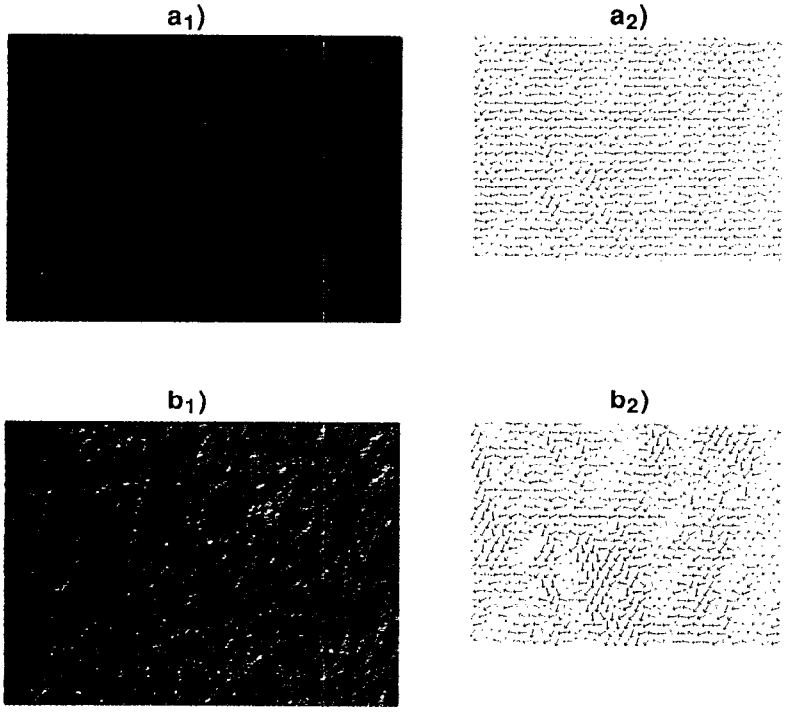

FIG. 14. Morphology of the magnetic state in a sample with 2-D random anisotropy, $H_k = 4000$ Oe, and $H_{xhg} = 300$ Oe. [The hysteresis loop for this sample is shown in Fig. 10(d); note that $H_c = 1315$ Oe.] Initially, the magnetization was saturated along the negative X axis. Frame (a) was obtained when the initial state was allowed to relax under an applied field of $H_x = -600$ Oe, yielding $\langle M_x \rangle = -0.9\, M_s$ for the average magnetization along X. The magnified view on the right shows the magnetization pattern in a small section of the lattice. Frame (b) represents the situation at $H_x = 800$ Oe, at which point $\langle M_x \rangle = -0.7\, M_s$. In (c) the applied field is 1155 Oe and $\langle M_x \rangle = -0.5\, M_s$. Frame (d) corresponds to $H_x = 1310$ Oe, where $\langle M_x \rangle \simeq 0$. In (e) the field is 1375 Oe and the average M_x is $0.5\, M_s$. Frame (f) shows the state of magnetization at $H_x = 1465$ Oe, where $\langle M_x \rangle = 0.9\, M_s$.

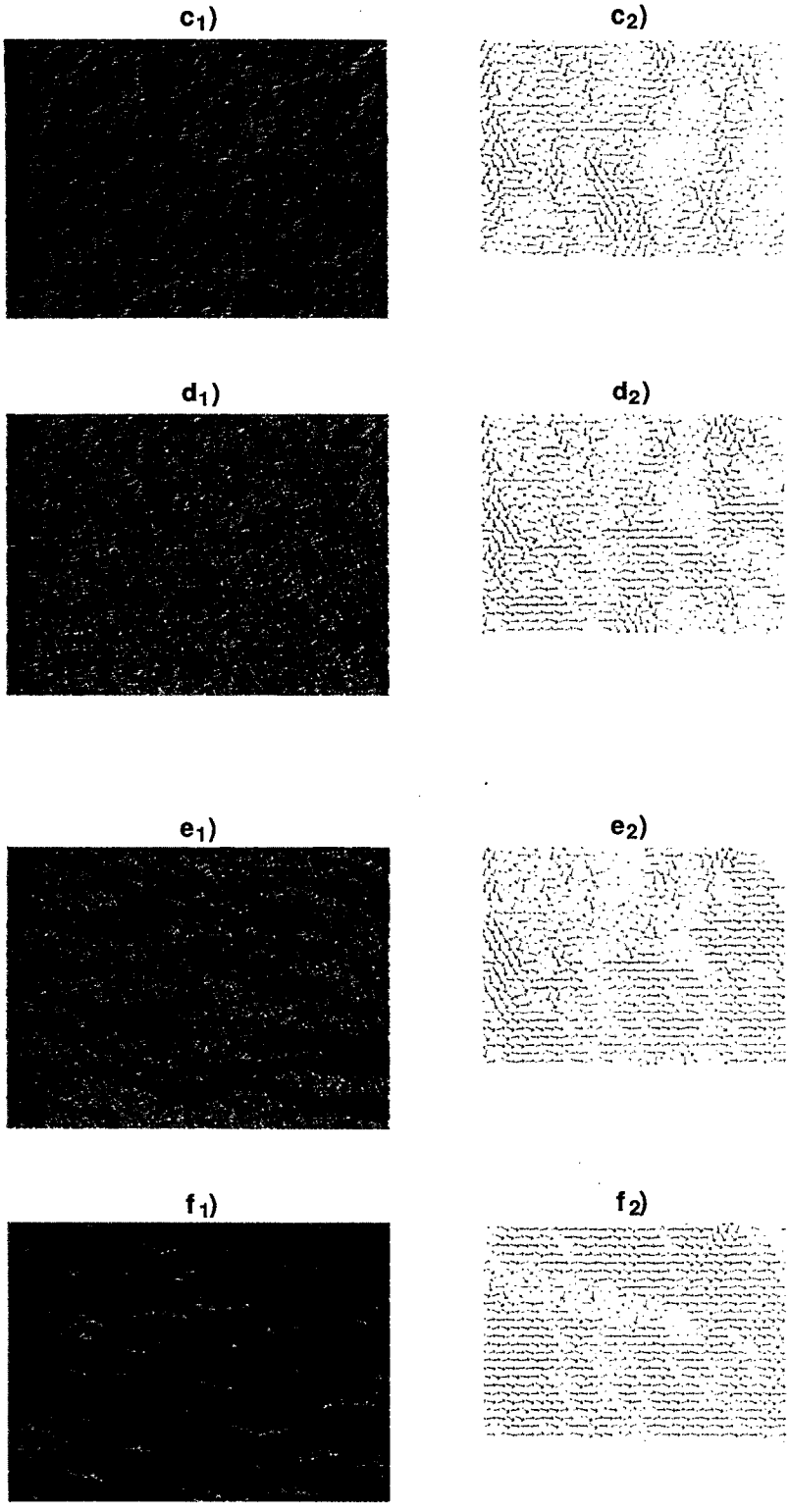

FIG. 14 (*Continued*)

netic moments during the reversal process depicted in Fig. 14. Here, the angles from 0° to 360° are divided into 36 bins, and the number of pixels associated with each bin is displayed on a polar plot. In Fig. 15(a) the applied field is large and along the negative X axis; that is why the angular distribution is concentrated around $\phi = 180°$. The state corresponding to Fig. 15(b) has the angles more widely spread, but they are still predominantly in the left half of the plane. Figure 15(c)–(e) shows that around the coercive field the moments rotate toward the right half of the

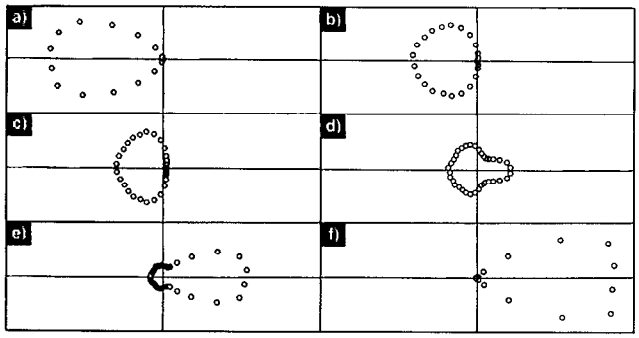

FIG. 15. Polar plots showing the angular distribution of magnetization in frames (a)–(f) of Fig. 14.

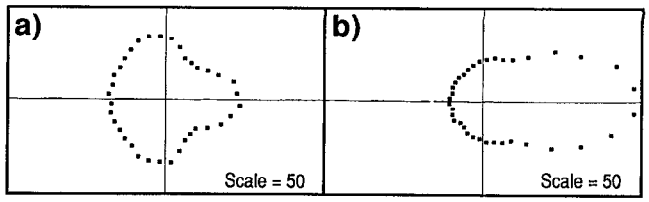

FIG. 17. Polar plots showing the angular distribution of magnetization in frames (a) and (b) of Fig. 16.

plane, making the polar plot more symmetric with respect to the vertical axis. The remaining plot shows the near-saturated state corresponding to a large value of the applied field.

C. Example 3

The patterns of magnetization during a loop-trace for a sample with 3-D random anisotropy, $H_k = 4000$ Oe and $H_{xhg} = 100$ Oe are shown in Fig. 16. [This sample's hysteresis loop is shown in Fig. 11(b).] The patterns in (a) and (b) correspond to the applied fields of 1050 and 1150 Oe, respectively. (a1) and (b1) represent the state of magnetization in the entire 256×256 lattice, using the same coloring scheme as in Fig. 14. In (a2) and (b2), which are magnified views of a small region of the lattice, the color code is different. Here, the color depicts the strength of local vorticity ζ at each pixel; ζ is defined as follows:

$$\zeta = \frac{1}{6} \sum_{i=1}^{6} \mathbf{u}_i \times \frac{\mathbf{m}_i}{|\mathbf{m}_i|}, \tag{8}$$

where $\mathbf{u}_i$ are unit vectors pointing from a given pixel to each one of its six nearest neighbors, and $\mathbf{m}_i$ are the magnetization vectors of those neighbors. Clearly, $-1 \leqslant \zeta \leqslant +1$, with $\zeta = 1$ representing maximum counterclockwise vorticity, and $\zeta = -1$ corresponding to maximum clockwise vorticity. The color coding of ζ in frames (a2) and (b2) uses the color wheel of Fig. 7(b), with purple assigned to $+1$, red to -1, and the colors in between purple and red sequentially assigned to values of ζ between $+1$ and -1. These frames show arrows which represent the magnetization of each pixel, but, in addition, the color of each arrow shows the strength of vorticity in its neighborhood. Red and purple arrows are strongly vortex like,

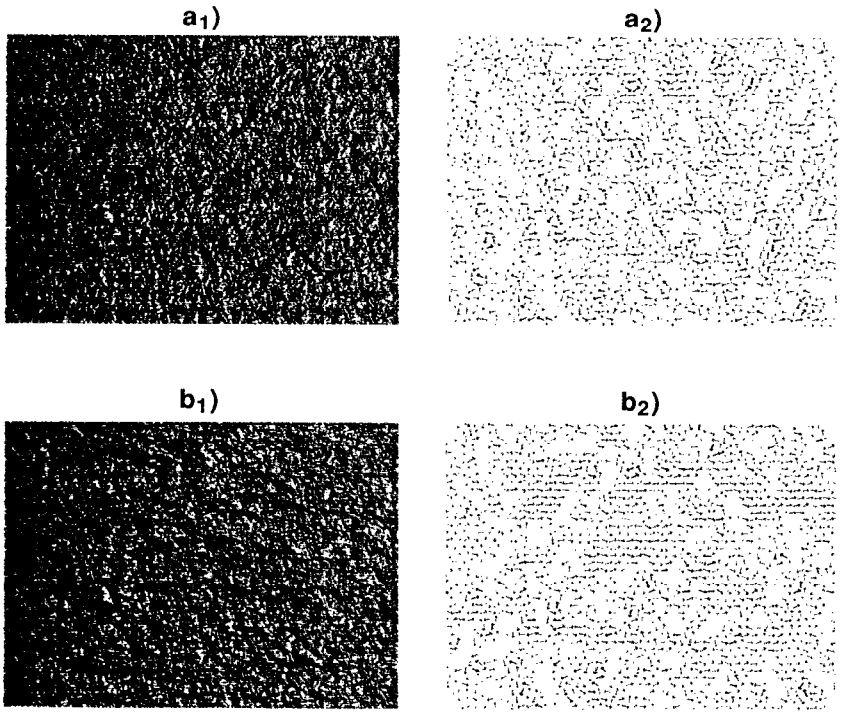

FIG. 16. Morphology of the magnetic state in a sample with 3-D random anisotropy, $H_k = 4000$ Oe, and $H_{xhg} = 100$ Oe. The initial state was saturated along $-X$, and the applied field was scanned (in discrete steps) along X in order to trace the hysteresis loop. [The loop for this sample is shown in Fig. 11(b); note that $H_c = 1040$ Oe.] (a) State of magnetization at $H_x = 1050$ Oe, just above the coercivity. For the frame on the left the color code shows the direction of local magnetization. The magnified view on the right is from a small section of the lattice, but the arrows are colored according to the strength of vorticity ζ in their immediate neighborhood. Purple represents the largest counterclockwise vorticity, while red corresponds to the largest clockwise vorticity. (b) The state of magnetization at $H_x = 1150$ Oe, where $\langle M_x \rangle = 0.35\ M_s$. Again, the magnified view on the right is color-coded according to the strength of vorticity ζ.

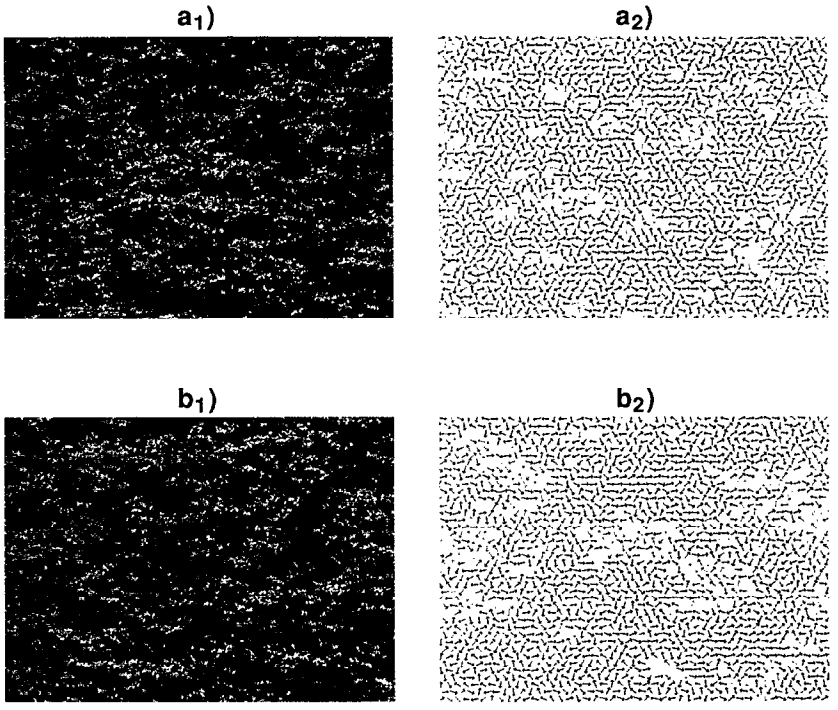

FIG. 18. (a) State of magnetization at $H_x = 1050$ Oe relative to the state at $H_x = 1100$ Oe for the sample described in Fig. 16. The purple pixels are the ones that do not change as the field goes from 1050 to 1100 Oe, whereas the red pixels rotate by 180°. The magnified view on the right is from a small section of the lattice. (b) State of magnetization at $H_x = 1100$ Oe relative to the state at $H_x = 1150$ Oe.

whereas green pixels have no vorticity at all.

Figure 17 shows the angular distribution of magnetization for the two states depicted in Fig. 16. Figure 18 shows the change in the state of magnetization as the field is increased, first from 1050 to 1100 Oe and then from 1100 to 1150 Oe. Here, the color of each pixel represents the dot product of local magnetization directions between two states. As before, purple is $+1$, red is -1, and the colors in between represent intermediate values of the dot product. Clearly, most dipoles in the lattice remain stationary as the field is increased from 1050 to 1100 Oe [Fig. 18(a)] and then from 1100 to 1150 Oe [Fig. 18(b)]. This is evi-

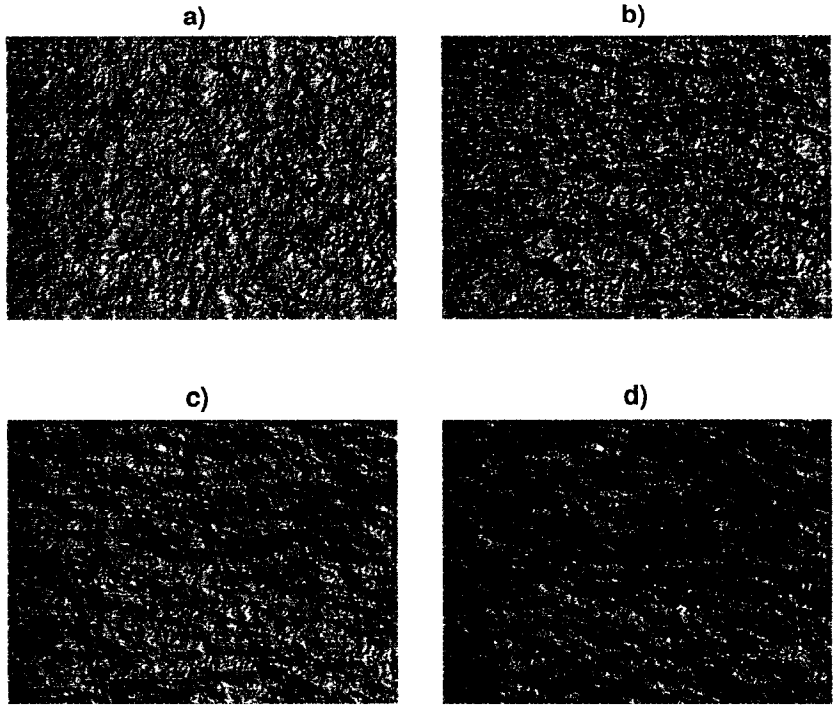

FIG. 19. Morphology of the magnetic state near the coercive field in a sample with 3-D random anisotropy, $H_x = 4000$ Oe, and $H_{xhg} = 200$ Oe. The initial state was saturated in the $-X$ direction, and the applied field was scanned (in discrete steps) along X in order to trace the hysteresis loop. [The loop for this sample is shown in Fig. 11(c); note that $H_c = 1010$ Oe.] Color depicts the direction of local magnetization. (a) The state of magnetization at $H_x = 1000$ Oe, just below coercivity. The average magnetization along X is $\langle M_x \rangle = -0.1\, M_s$. (b) At $H_x = 1050$ Oe, where $\langle M_x \rangle = 0.27\, M_s$. (c) At $H_x = 1100$ Oe, where $\langle M_x \rangle = 0.6\, M_s$. (d) At $H_x = 1150$ Oe, where $\langle M_x \rangle = 0.77\, M_s$.

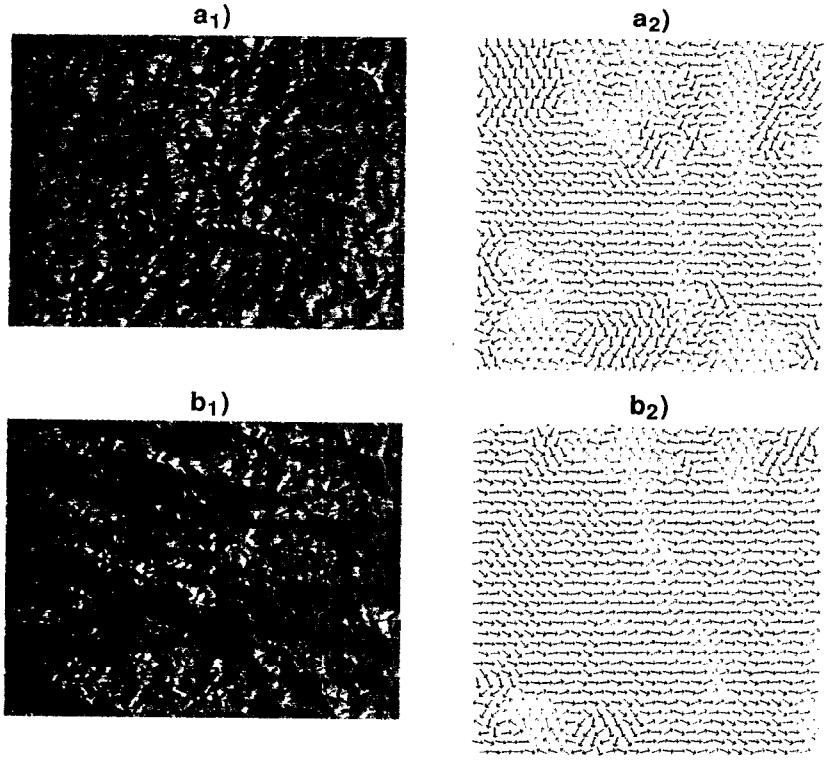

FIG. 20. Morphology of the magnetic state in a sample with 2-D random anisotropy, $H_k = 4000$ Oe, and $H_{xhg} = 500$ Oe. The initial state was saturated in the $-X$ direction, and the applied field was scanned continuously along X (rate = 20 Oe/ns) in order to trace the hysteresis loop. [The loop for this sample is shown in Fig. 10(f); note that $H_c = 1005$ Oe.] (a) The state of magnetization at $H_x = 980$ Oe, just below coercivity, where $\langle M_x \rangle = -0.17\, M_s$. Shown on the right is the magnified view of a small section of the lattice. (b) The state of magnetization at $H_x = 1080$ Oe, where $\langle M_x \rangle = +0.55\, M_s$.

denced by the abundance of purple pixels in these frames. Red pixels are the ones which have rotated by 180°, yellow pixels have rotated by 90°, and so on. Frames (a2) and (b2) are magnified views of a small region from the full frames in (a1) and (b1); in addition to local magnetization vectors, these frames show the color-coded dot product of each vector with the same vector in a subsequent state.

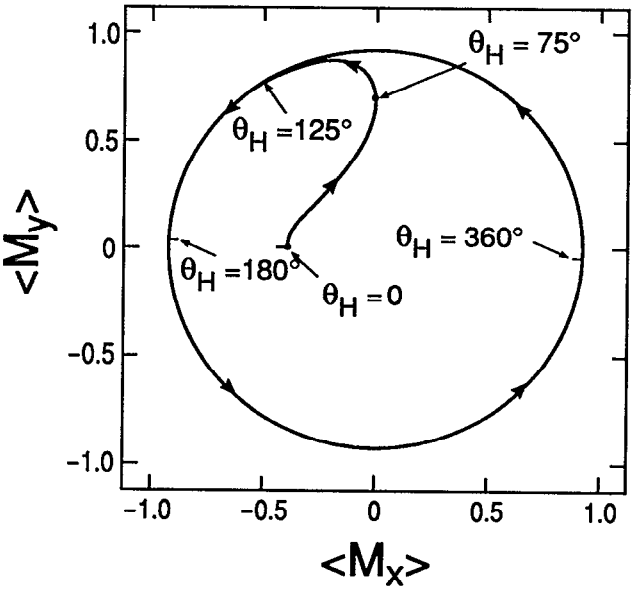

FIG. 21. Simulation of a rotating field in the plane of a sample with 3-D random anisotropy, $H_k = 4000$ Oe and $H_{xhg} = 300$ Oe. The applied field $\mathbf{H}_{ext}$ has a fixed magnitude of 840 Oe, and its angle with the positive X axis is denoted by Θ_H. The graph depicts the behavior of $\langle M_y \rangle$ versus $\langle M_x \rangle$ as the field rotates through 720 deg.

D. Example 4

The reverse-magnetized "fingers" created during the loop-trace become more pronounced when the exchange interaction between neighboring lattice cells increases. This can be seen by comparing Fig. 19 with Fig. 20, which show the states of magnetization in the neighborhood of the coercive field for two samples with different intergranular exchange coefficients. The sample depicted in Fig. 19 has $H_{xhg} = 200$ Oe and 3-D random anisotropy, while that in Fig. 20 has $H_{xhg} = 500$ Oe and 2-D random anisotropy; both samples have $H_k = 4000$ Oe. The much thicker fingers in Fig. 20 are due to the latter sample's larger value of H_{xhg}, and not, as the skeptic might argue, caused by the differences in the distributions of the anisotropy axes. Further proof of this point is provided by comparing Fig. 19 with Fig. 16 (or Fig. 20 with Fig. 14), where the only difference between the samples is the value of H_{xhg}.

E. Example 5

In order to understand the results of torque magnetometry on the media of magnetic recording, the sample with 3-D random anisotropy, $H_k = 4000$ Oe and $H_{xhg} = 300$ Oe, was subjected to a rotating field. [From the corresponding loop in Fig. 11(d) the coercivity of this sample is known to be about 850 Oe.]

The sample was initially saturated in the negative X direction with a field $H_x = -2000$ Oe. It was then relaxed, while H_x increased to $+840$ Oe (just below coercivity) at the fixed rate of 20 Oe/ns. The sample was allowed

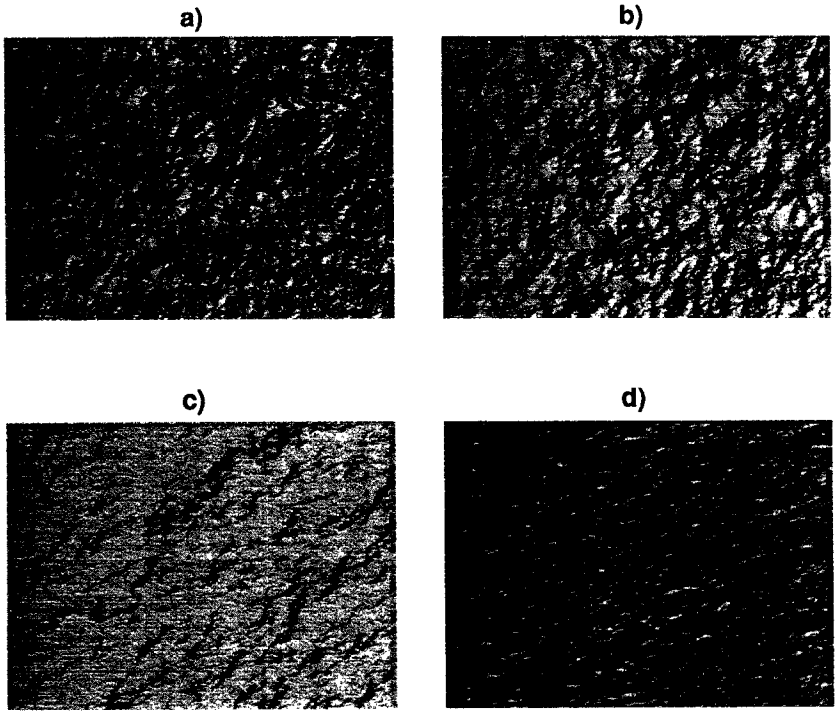

FIG. 22. Morphology of the magnetic state during the rotating field experiment described in the caption to Fig. 21. Each frame shows the pattern of magnetization distribution at a particular angle Θ_H of $\mathbf{H}_{ext}$. (a) $\Theta_H = 0$; (b) $\Theta_H = 35°$; (c) $\Theta_H = 85°$; and (d) $\Theta_H = 135°$.

to relax further while the field remained along the X axis with the fixed magnitude of 840 Oe. During this phase of the simulation, the applied field remained parallel to the X axis and, at the end, the sample was in a state with $\langle M_x \rangle \simeq -0.4\, M_s$ and $\langle M_y \rangle \simeq 0$. At this point the magnitude of the field was fixed ($H_{ext} = 840$ Oe) and it began to rotate counterclockwise in the plane of the sample at the rate of 10° per nanosecond. (Θ_H shall denote the angle between $\mathbf{H}_{ext}$ and the positive X axis.) As the field rotated, the magnetization was relaxed following the LLG dynamics. Figure 21 shows the plot of $\langle M_y \rangle$ vs $\langle M_x \rangle$, obtained during the rotation process; on this graph, the starting point for the rotation of $\mathbf{H}_{ext}$ is marked as $\Theta_H = 0$. Note that by the time $\Theta_H = 125°$, the average magnetization vec-

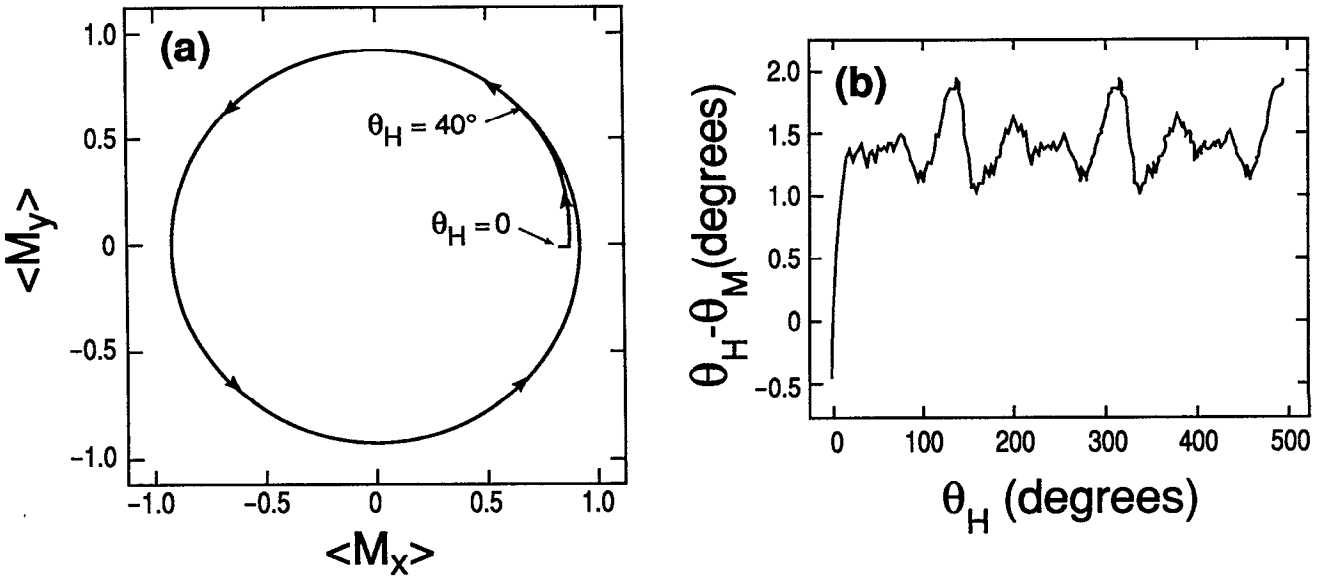

FIG. 23. Simulation of a rotating field experiment in the plane of a sample with 3-D random anisotropy, $H_k = 4000$ Oe and $H_{xhg} = 300$ Oe. The applied field $\mathbf{H}_{ext}$ has a fixed magnitude of 1050 Oe, and its angle with the positive X axis is denoted by Θ_H. (a) Plot of $\langle M_y \rangle$ vs $\langle M_x \rangle$ as the field rotates through 500 deg. (b) The angle between $\langle \mathbf{M} \rangle$ and $\mathbf{H}_{ext}$ as function of Θ_H.

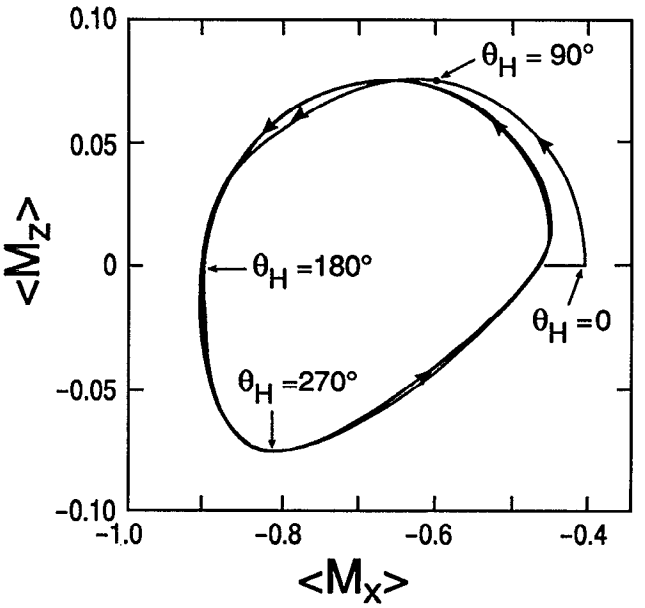

FIG. 24. Simulation of a rotating field out of the plane of a sample with 3-D random anisotropy, $H_k = 4000$ Oe and $H_{xhg} = 300$ Oe. The applied field $\mathbf{H}_{ext}$ has a fixed magnitude of 840 Oe, and, as it rotates counterclockwise in the XZ plane, its angle with the positive X axis is denoted by Θ_H. The graph depicts the behavior of $\langle M_z \rangle$ vs $\langle M_x \rangle$ as the field rotates through 1000 deg.

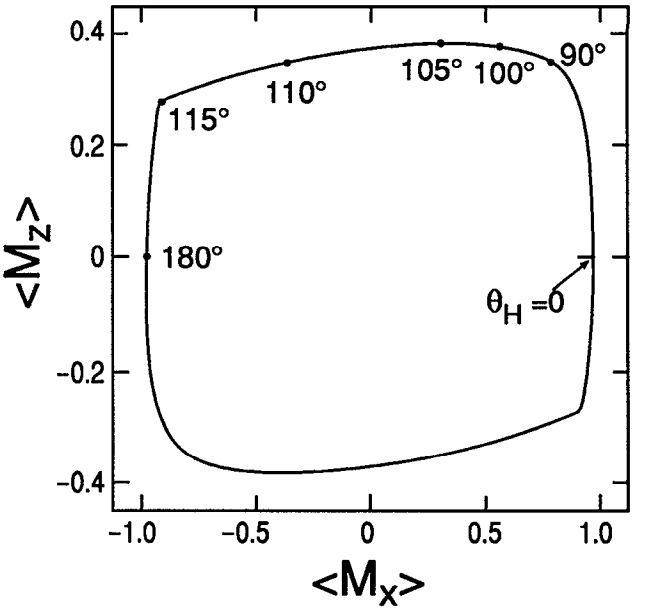

FIG. 26. Simulation of a rotating field out of the plane of a sample with 3-D random anisotropy, $H_k = 4000$ Oe and $H_{xhg} = 300$ Oe. The applied field $\mathbf{H}_{ext}$ has a fixed magnitude of 4000 Oe, and, as it rotates counterclockwise in the XZ plane, its angle with the positive X axis is denoted by Θ_H. The graph depicts the behavior of $\langle M_z \rangle$ vs $\langle M_x \rangle$ as the field rotates through 720 deg.

tor $\langle \mathbf{M} \rangle$ (i.e., $\langle M_x \rangle \hat{x} + \langle M_y \rangle \hat{y}$) is nearly saturated ($\langle M \rangle = 0.93\, M_s$) and is rotating close behind the field. The morphology of the magnetic state at several instances of this simulated torque experiment is shown in Fig. 22. The color represents the direction of local magnetization. Notice that the fingerlike domains rotate with the field in such a way as to keep their long axes more or less aligned with $\mathbf{H}_{ext}$. What is interesting here is that a field, whose magnitude is just about the coercivity of the sample, can make the magnetization follow it so well.

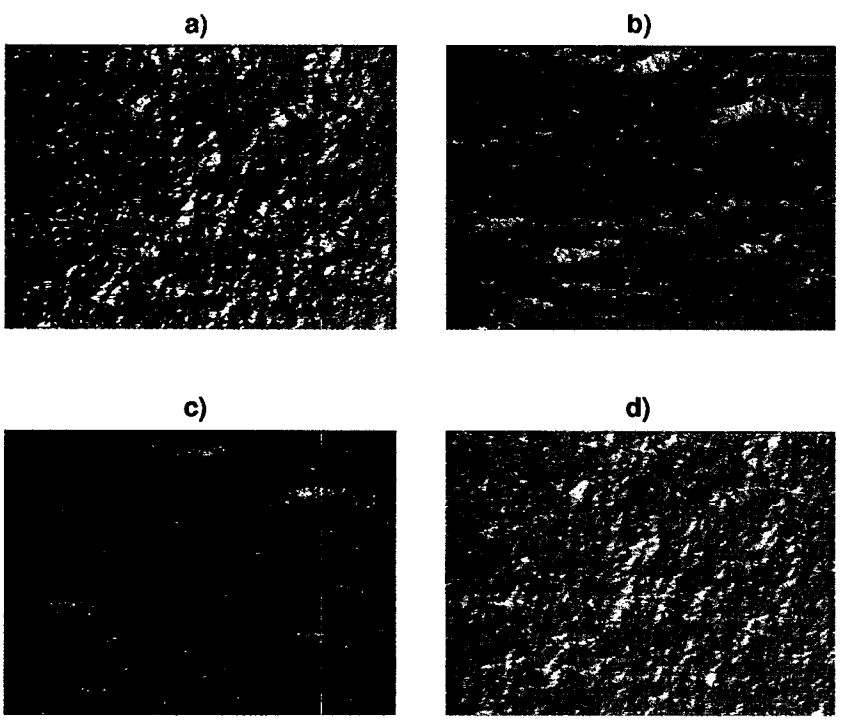

FIG. 25. Morphology of the magnetic state during the rotating field experiment described in the caption to Fig. 24. Each frame shows the pattern of magnetization distribution at a particular angle Θ_H of $\mathbf{H}_{ext}$. (a) $\Theta_H = 0$; (b) $\Theta_H = 135°$; (c) $\Theta_H = 180°$; and (d) $\Theta_H = 360°$.

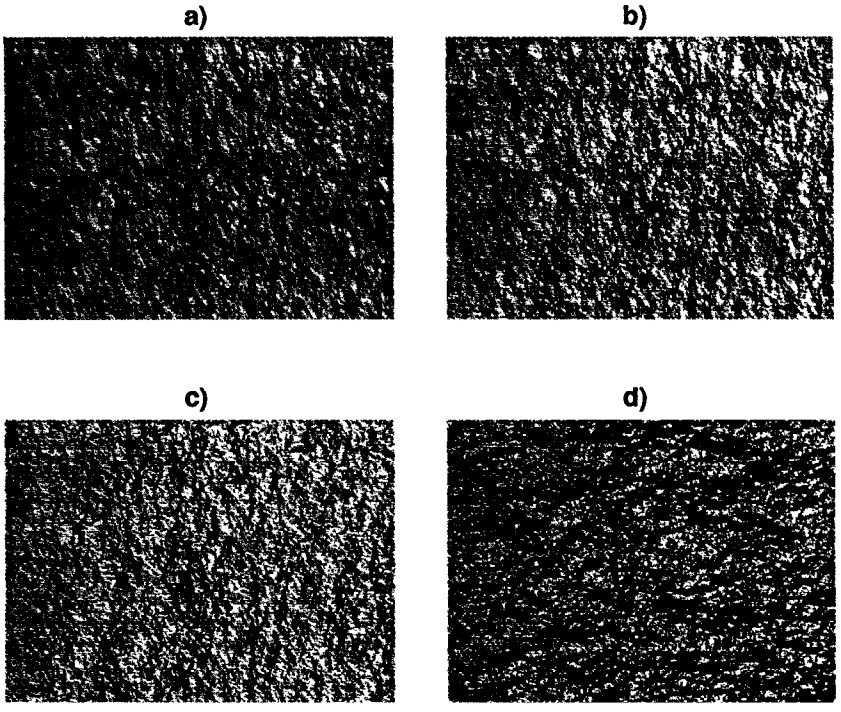

FIG. 27. Morphology of the magnetic state during the rotating field experiment described in the caption to Fig. 26. Each frame shows the pattern of magnetization distribution at a particular angle Θ_H of $\mathbf{H}_{ext}$. (a) $\Theta_H = 90°$; (b) $\Theta_H = 100°$; (c) $\Theta_H = 105°$; and (d) $\Theta_H = 110°$.

The same simulation as above was repeated, but this time the field was brought to $H_x = +1050$ Oe (well above coercivity) before the rotation began. Figure 23(a) shows the plot of $\langle M_y \rangle$ vs $\langle M_x \rangle$ during this rotation process. The magnetization of the sample is now almost fully saturated ($\langle M \rangle = 0.94\ M_s$) and, as the plot of $\Theta_H - \Theta_M$ in Fig. 23(b) shows, $\langle \mathbf{M} \rangle$ follows the external field very closely. These results should not come as a surprise, considering that the anisotropy axes are randomly distributed, leaving the sample without any particular direction of anisotropy in the XY plane.

Results of simulations in which the applied field rotat-

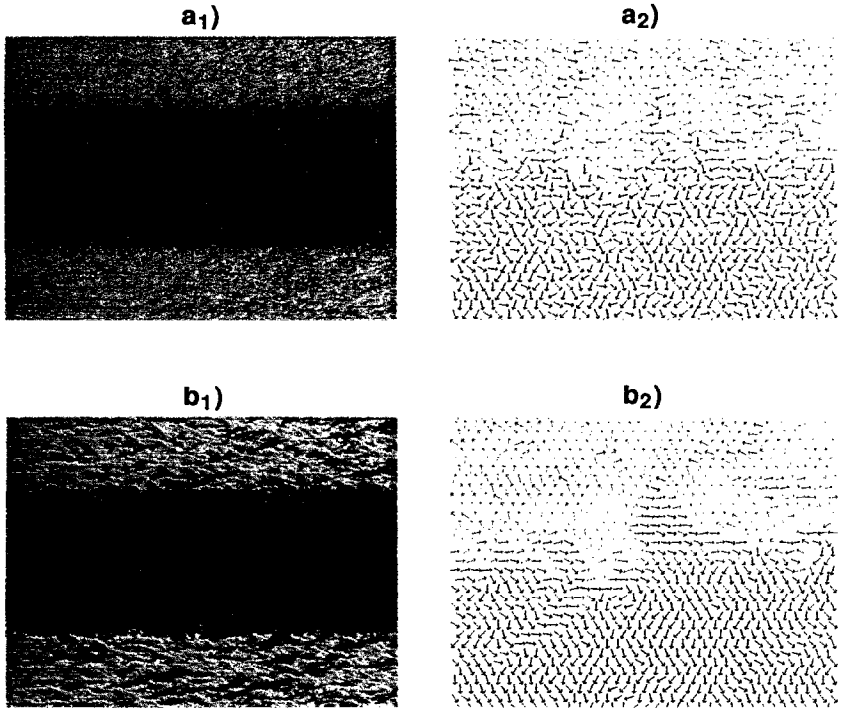

FIG. 28. Pair of head-to-head walls in medium with 2-D random anisotropy and $H_k = 4000$ Oe. For the sample depicted in (a) $H_{xhg} = 100$ Oe, while the sample in (b) has $H_{xhg} = 500$ Oe. The walls are parallel to X, and the magnetization was initially set to be either parallel to Y (green) or antiparallel to Y (purple). The initial state was then relaxed, resulting in the steady-state magnetization patterns shown in (a) and (b). Each closeup on the right-hand side shows a section from the (relaxed) upper wall.

ed out of the plane of the sample are reported next. Here again, an in-plane field along the negative X was initially applied to the sample. The field was scanned from -2000 Oe to $+840$ Oe at the rate of 20 Oe/ns. At this point the field was fixed, and the sample was allowed some more time to fully relax. The field was then rotated out of the plane of the sample (in the XZ plane) at the rate of 10 deg/ns. Figure 24 is a plot of $\langle M_z \rangle$ vs $\langle M_x \rangle$ during this rotation process. Because of strong demagnetizing effects ($4\pi M_s = 11.3$ kOe) the magnetization cannot follow the field too far out of the plane of the sample. That is why $\langle M_z \rangle$ in Fig. 24 is at most about 0.08 M_s. However, when $\Theta_H = 180°$, the applied field can bring the sample close to saturation ($\langle M \rangle \simeq 0.91\, M_s$). After that the pattern repeats itself. The morphology of the magnetic state of the sample during this rotating field experiment is shown in Fig. 25.

We repeated the above experiment with an applied field of 4000 Oe; the resulting graph of $\langle M_z \rangle$ versus $\langle M_x \rangle$ is shown in Fig. 26. Now, $\langle M_z \rangle$ can reach a maximum of 0.39 M_s, which is understandable in terms of the demagnetizing effects; random distribution of the anisotropy axes in 3 D does not allow this experiment to reveal the strength of H_k. The morphology of the magnetic state during this rotating field experiment is shown in Fig. 27.

F. Example 6

In longitudinal magnetic recording the recorded domains form high-energy head-to-head walls. The demagnetizing force causes these walls to become jagged, resulting in a structure that contributes significantly to the readout noise. In this example, we study the patterns of such domain walls. Figure 28(a) shows a pair of head-to-head walls in a sample with 2-D random anisotropy, $H_k = 4000$ Oe, and $H_{xhg} = 100$ Oe. A reverse-magnetized stripe with sharp walls was initially created on the lattice, and the system was allowed to relax following the LLG dynamics. Frame (a_1) shows the magnetization of the entire lattice in the relaxed state, while (a_2) is a closeup of the upper wall. Figure 28(b) is similar to 28(a), except for the value of H_{xhg} which is 500 Oe. The jagged edges of the walls and the complex patterns of magnetization are reminiscent of real films photographed with high resolution Lorentz electron microscopy.

We also studied a different kind of structure in which we allowed the grains to be irregular and deviate from a single-domain-particle behavior. The lattice constant d was reduced to 50 Å, and random patches were selected on the lattice [see Fig. 29(a)]. All the cells have $M_s = 900$ emu/cm^3 and $H_k = 4000$ Oe. Cells inside any given patch had the same axes of anisotropy, but from patch to patch the anisotropy axis varied randomly in 2 D. Inside each patch the exchange field between neighboring cells was $H_{xhg} = 600$ Oe (corresponding to $A_x \simeq 10^{-7}$ erg/cm), but at the patch borders H_{xhg} was reduced to 200 Oe. Figure 29(b) shows the initial state of the lattice, with a reverse-magnetized stripe in the middle, and with the patch-

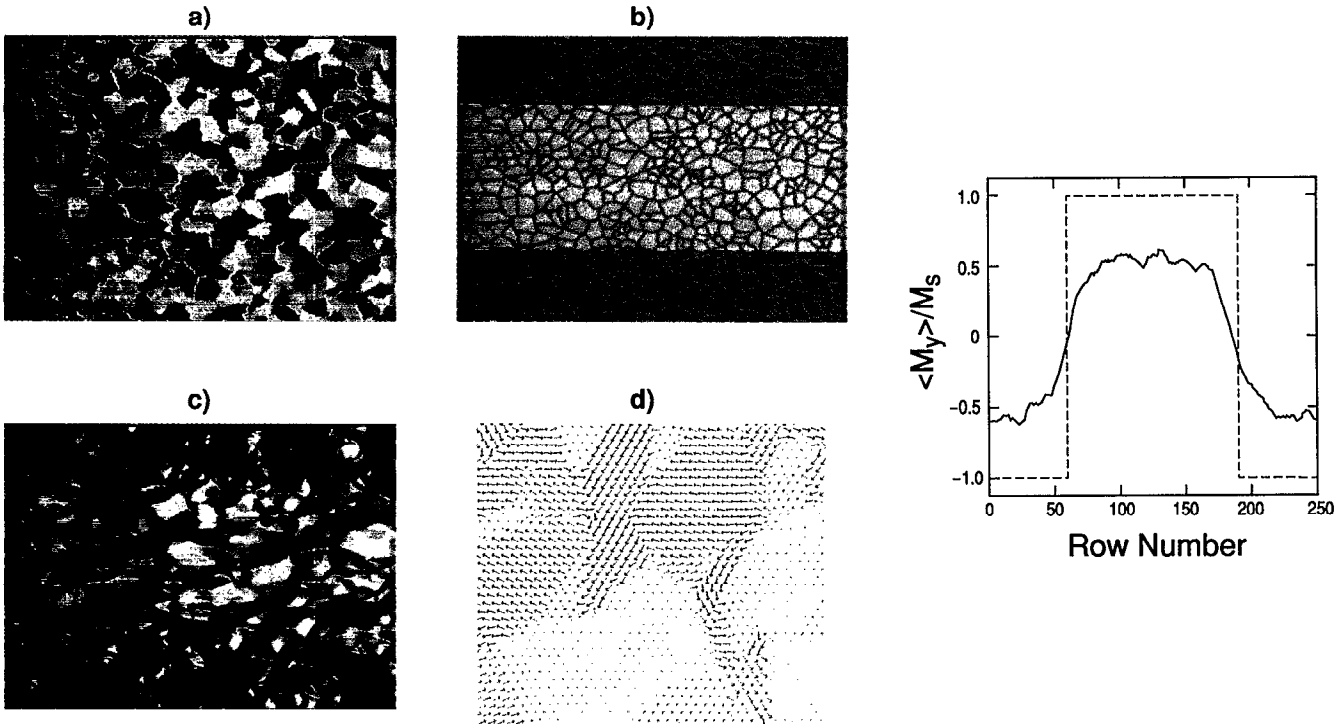

FIG. 29. Pair of head-to-head walls in a medium with 664 patches, 2-D random anisotropy (patch to patch), $H_k = 4000$ Oe, $H_{xhg} = 600$ Oe within the patches, and $H_{xhg} = 200$ Oe at the patch borders. Note that since the lattice constant d is only 50 Å in this case, the total lattice area is $1.28 \times 1.11\ \mu m^2$. (a) Color-coded distribution of the axes of anisotropy. Since a given patch has a unique easy axis, the color also identifies the patch. (b) The initial state of magnetization, showing a reverse-magnetized stripe with sharp domain walls. Superimposed on this picture are the patch borders, shown in gray. (c) Final state of the lattice upon relaxation in zero applied field, using the LLG dynamics. (d) Closeup of a small section of the relaxed upper wall. (e) Averaged magnetization over each row of the lattice, plotted versus the row number, before (- - -) and after (— —) relaxation.

borders superimposed in gray. The state of the lattice after relaxation is shown in Fig. 29(c), with a closeup in frame (d). Jagged walls and internal domain structure are clearly observed in this picture. The magnetization along Y(averaged over each row) is plotted in Fig. 29(e). From this figure it is clear that the relaxed domain is somewhat broadened, and that its average magnetization has decreased by more than 40%.

V. CONCLUDING REMARKS

Micromagnetic simulations of the longitudinal recording media reported in this paper focused on the properties of the hysteresis loops and torque curves, their dependence on material parameters, and the morphology of the magnetization state. Among other things, we observed the following:

(i) The magnetization distribution in the remanent state has ripples similar to those observed experimentally.

(ii) The process of reversal under an applied field begins with the formation of vortices which act as nucleation centers, and continues with the growth of elongated domains. These domains are oriented with their long axes along the direction of the applied field.

(iii) The coercivity squareness S^* of the loops increases with increasing strength of the exchange interaction.

There exists a large number of interesting problems related to the micromagnetics of thin film recording media which can be tackled by computer simulations of the type reported in this paper. Here, we did not attempt to address all these problems, instead, we focused on a few representative cases and tried to demonstrate the power of the simulation technique as a tool for analysis, as well as the richness and variety of information that can be obtained with present-day computers. As the magnetic recording densities increase, and the minute features of domains and walls gain relevance and significance, large-scale computer simulations will become indispensable tools for the study of the "nanomagnetics" of the recording media.

ACKNOWLEDGMENTS

This work has been supported by the IBM Corporation. The authors thank Dr. T. Yogi, Dr. I. McFadyen, Dr. T. Nguyen, and Dr. V. Speriosu of the IBM Almaden Research Center for sharing their experimental data and for many valuable discussions during the course of this project.

REFERENCES

1. T. Yogi, C. Tsang, T. A. Nguyen, K. Ju, G. L. Gorman, and G. Castillo, IEEE Trans. Magn. **26**, 2271–2276 (1990).
2. J. N. Chapman, J. Phys. D **17**, 623–647 (1984).
3. T. A. Nguyen, I. R. McFadyen, C. Hwang, and P. S. Alexopoulos, J. Phys. Colloq. C8, Tome **49**, 1995–1996 (1988).
4. D. Rugar, H. J. Mamin, and P. Guthner, Appl. Phys. Lett. **55**, 2588 (1989).
5. G. F. Hughes, J. Appl. Phys. **54**, 5306–5313 (1983).
6. M. Mansuripur, J. Appl. Phys. **63**, 5809 (1988).
7. M. Mansuripur and R. Giles, Comput. Phys. **4**, 291–302 (1990).
8. J-G Zhu and H. N. Bertram, J. Appl. Phys. **63**, 3248 (1988).
9. W. D. Hillis and G. Steele, Commun. ACM **29**, 1170 (1986).
10. L. W. Tucker and G. G. Robertson, IEEE Comput. Magn. **10**, 26 (1988).
11. B. K. Middleton, "The Recording and Reproducing Processes," in *Magnetic Recording*, edited by C. D. Mee and E. D. Daniel (McGraw-Hill, New York, 1987), Vol. 1, Chap. 2.
12. T. Yogi, T. A. Nguyen, S. E. Lambert, G. L. Gorman, and G. Castillo, IEEE Trans. Magn. **26**, 1578–1580 (1990).
13. T. Chen and T. Yamashita, IEEE Trans. Magn. **24**, 2700 (1988).
14. T. Yogi, G. L. Gorman, C. Hwang, M. A. Kakalec, and S. E. Lambert, IEEE Trans. Magn. **24**, 2727 (1988).
15. T. Yogi, T. Nguyen, S. E. Lambert, G. L. Gorman, M. A. Kakalec, and G. Castillo, Paper BA-09, presented at the MMM'90 Conference, San Diego, CA; abstract published in J. Appl. Phys. **69**, 4749 (1991).
16. J. K. Howard, J. Vac. Sci. Technol. A **3**, 657–658 (1985).
17. N. R. Belk, P. K. George, and G. S. Mowry, IEEE Trans. Magn. **21**, 1350–1355 (1985).
18. N. R. Belk, P. K. George, and G. S. Mowry, J.Appl. Phys. **59**, 557–563 (1986).
19. P. S. Alexopoulos and R. H. Geiss, IEEE Trans. Magn. **22**, 566–569 (1986).
20. J. A. Thornton, J. Vac. Sci. Technol. A **4**, 3059 (1986).
21. P. S. Alexopoulos and T. C. O'Sullivan, Annu. Rev. Mater. Sci. **20**, 391–420 (1990).
22. I. R. McFadyen and I. A. Beardsley, J. Appl. Phys. **67**, 5540–5543 (1990).
23. L. Landau and E. Lifshitz, Phys. A. Sov. Union **8**, 153 (1935).
24. T. L. Gilbert, Phys. Rev. **100**, 1243 (1955).
25. C. C. Shir, J. Appl. Phys. **49**, 3413 (1978).
26. A. P. Malozemoff and J. C. Slonczewski, *Magnetic Domain Walls in Bubble Materials* (Academic, New York, 1979).
27. R. Giles and M. Mansuripur, J. Mag. Soc. Japn. **15**, Supplement No. S1, 299–306 (1991).
28. M. Mansuripur and R. Giles, IEEE Trans. Magn. **24**, 2327 (1988).
29. M. Mansuripur, J. Appl. Phys. **66**, 3731 (1989).
30. M. E. Schabes and A. Aharoni, IEEE Trans. Magn. **23**, 3882 (1987).